Electrochimica Acta 388 (2021) 138645

Contents lists available at ScienceDirect

Electrochimica Acta

journal homepage: www.elsevier.com/locate/electacta

High-performance Li-S batteries enabled by polysulfide-infiltrated free-standing 3D carbon cloth with CeO_2 nanorods decoration

Zhen Wei, Junhao Li, Yifan Wang, Ruigang Wang*

Department of Metallurgical and Materials Engineering, The University of Alabama, Tuscaloosa, AL 35487, United States

ARTICLE INFO

Article history:
Received 1 March 2021
Revised 20 April 2021
Accepted 15 May 2021
Available online 22 May 2021

Keywords:
Li-S batteries
Cerium oxide nanorods
Shuttle effect
Carbon cloth
Polysulfide adsorption

ABSTRACT

To achieve scale-up commercialization of Li-S batteries, parasitic shuttle effect, leading to low utilization of active material and fast capacity decay, has to be resolved effectively. Herein, we prepared CeO_2 nanorods decorated interwoven 3-D carbon cloth via facile one-step hydrothermal reaction and Li_2S_6-containing polysulfide as starting material to successfully improve the electrochemical performance of Li-S battery. First, strong chemical interaction toward polysulfides was successfully constructed by polar CeO_2 nanorods and numerous oxygen vacancies on their surface acting as efficient polysulfides anchoring sites significantly enhanced the utilization of active material sulfur. Second, interwoven freestanding carbon cloth can considerably enhance redox kinetics through a 3-D interconnected network with abundant long-range electron transfer channels and can significantly improve redox kinetics by easy accessibility to electrolyte and abundant ion transport pathways. Third, the utilization of Li_2S_6-containing catholyte leads to uniform distribution of active material and improves sulfur utilization. Benefiting from the aforementioned advantages, free-standing 3-D carbon cloth with CeO_2 nanorods decoration combined with Li_2S_6-containing catholyte (CC@CeO_2@Li_2S_6) electrode delivered an initial discharge capacity of 1311 mA h g^{-1} at 0.2C and approximately 95% of the initial discharge capacity was remained after 100 galvanostatic cycles, manifesting superior capacity retention with minimal capacity fading of 0.050% per cycle.

1. Introduction

Lithium ion batteries (LIBs) are promising candidates among the existing energy storage devices due to extensive utilization in the secondary battery field [1]. LIBs not only have been dominant rechargeable power sources in portable electrical devices market since it was initially launched in early 1990s [2], but also have revolutionized the transportation industry from conventional fossil fuels powered vehicles to battery powered electric vehicles. However, conventional LIBs consisting of insertion-compound cathodes (e.g. $LiCoO_2$, $LiMnO_4$, and $LiFePO_4$) and graphite anode have been demonstrated to reach their maximal theoretical specific capacity of 300 mAh g^{-1} and maximal theoretical energy density of 150–200 Wh kg^{-1} [3], so little exploration room considerably hinders the fulfillment of increasing demands of electric vehicles and smart grids [4]. The lithium-sulfur (Li-S) battery has been receiving increasing attention from scientific community due to its remarkable properties such as considerable abundance of sulfur, nontoxic nature, and environmental friendliness. It is worth mentioning that its ultrahigh theoretical capacity (1675 mAh g^{-1}) and theoretical energy density (2600 Wh kg^{-1}) when coupled with lithium metal anode differentiate it from other conventional cathode materials [5]. Although rapid development of the Li-S battery resulting from substantial effort has been achieved, several formidable technical issues make the realization of commercialization a real challenge, including shuttle effect caused by polysulfide diffusion, poor conductivity of sulfur, and volume variation of the electrode during charge-discharge cycling process [6,7]. The shuttle effect, leading to rapid capacity decay and huge degradation of the cell electrochemical performance, is one of the most serious problems that the Li-S battery system is facing and has to be addressed urgently.

Over the past few years, a considerable amount of effort has been devoted to developing and engineering novel materials to address those aforementioned technical issues. Those synthesized cathode composites from previously reported work are generally classified into two categories (non-polar and polar materials) based on different working mechanisms to mitigate the shuttle effect of soluble lithium polysulfides. At the beginning, various carbonaceous nanomaterials were extensively exploited to inhibit parasitic dissolution of intermediate polysulfide species formed during charge-discharge cycling process due to remarkable physical confining capability against polysulfides. It is also worth mentioning that carbonaceous nanomaterials with excellent electronic conduc-

* Corresponding author.
E-mail address: rwang@eng.ua.edu (R. Wang).

https://doi.org/10.1016/j.electacta.2021.138645
0013-4686/

tivity can effectively facilitate electron transfer, resulting in fast redox kinetics for the Li-S battery. Abundant non-polar carbon architectures were developed including 0D microporous/mesoporous carbon particles, 1D carbon nanomaterials like multi-walled carbon nanotube (MWCNT) and 2D nanostructured carbon materials like graphene. For example, Wang et al. [8] reported that an innovative and facile synthesis of ordered mesoporous carbon with excellent conductivity and high specific surface area (1432 m^2 g^{-1}) was achieved by a simultaneous template and carbonization approach without the addition of metallic catalysts. Chen et al. [9] reported that a cost-effective and well-performed design of hierarchically structured MWCNT/S nanosphere with the collective effect of large pores as well as the existence of carboxyl functional groups can significantly improve the overall electrochemical performance of the Li-S battery. Zhang et al. [10] reported that a significant improvement of overall performance of the cell was fulfilled by an innovatively prepared sulfur anchored graphene composite through a cost-effective one-pot hydrothermal approach. The obtained results show that NanoS@G composite delivered an excellent discharge capacity of 1400 mAh g^{-1} for the first cycle, leading to high sulfur utilization of 83.7%. Moreover, the capacity was well maintained above 720 mAh g^{-1} over 100 cycles. The remarkable conducting nature, hierarchical structure and high porosity endow carbonaceous materials-based cathode with a superior initial discharge capacity, but subsequently the cell is usually followed by fast capacity fading. It is concluded that it is extremely hard for sulfur-carbon composites to maintain a stable and high capacity throughout the whole charge-discharge process due to the weak interaction between polar polysulfides and non-polar carbonaceous materials [11].

On the other side, the addition of polar materials in cathode has garnered considerable attention aiming at impeding the polysulfide diffusion. Various metal oxides (ZnO [12], Fe_3O_4 [13], V_2O_3 [14], TiO_2 [15], Ta_2O_5 [16], and MnO [17]) have been reported to effectively immobilize polysulfides, leading to increased sulfur utilization which is fulfilled by the presence of formed O^{2-} with a strong polar nature [18]. For example, Yuan et al. [19] used La_2O_3 nanoplates anchored highly conductive carbon nanotubes as a promising sulfur host to enhance the electrochemical performance of the cell. The optimal combination of highly conductive interconnected CNTs framework, that can provide abundant electron transfer pathways, and polar La_2O_3, that can successfully inhibit polysulfide diffusion and prevent irreversible loss of active material, endows the cell with superb initial discharge capacity of 1251 mAh g^{-1} and well-maintained capacity of 1011 mAh g^{-1} over 100 cycles at 0.1C. It is also worth noting that the innovatively synthesized composite exhibited superior capacity retention demonstrating capacity fading of 0.067% per cycle after 300 cycles at 0.1C.

In the meantime, CeO_2 has been used in cathode material preparation because CeO_2 can construct strong interaction with intermediate polysulfide species, successfully immobilizing polysulfides and ensuring excellent capacity retention. For example, Zhu et al. [20] reported that the combination of nano-sized sheet-like porous carbon with superb electrical conductivity and polar CeO_2 nanoparticles with excellent polysulfide-adsorbing capability provides the C/CeO_2/S composite with superb cyclability of 729 mAh g^{-1} over 300 cycles at 0.5C.

Comprehensive characterizations have also been used to confirm strong adsorption capability of CeO_2 against intermediate polysulfide species. For example, Wang et al. [21] reported that porous carbon nanofibers (CNF) with CeO_2 decoration was used as cathode matrix to enhance electrochemical performance. In their work, polysulfide adsorption test and UV–vis spectroscopy were employed to confirm the strong adsorption capability of CeO_2 against polysulfides and bare non-polar CNF was used as control group. Two distinct peaks corresponding to S_6^{2-} and S_4^{2-} species respectively were located at 411 nm and 280 nm, which can be clearly seen from the UV–vis spectra of the blank Li_2S_6-containing solution. Compared with bare non-polar CNF, a significant decrease in the peak intensity of those two peaks was realized by using synthesized CeO_2@CNF composite, demonstrating a great reduction in the concentration of polysulfide in CeO_2@CNF composite solution, which further exhibiting strong polysulfide adsorption capability by CeO_2.

Herein, we innovatively develop CeO_2 nanorods which are firmly anchored on free-standing carbon cloth via simple and facile one-step hydrothermal reaction and use Li_2S_6-containing polysulfide as starting material to effectively enhance electrochemical performance of Li-S battery. To the best of our knowledge, CeO_2 nanorods with numerous oxygen vacancies are used as efficient sulfur host material and effective polysulfides adsorbent for the first time. Elaborately fabricated CC@CeO_2@Li_2S_6 electrode delivered a superb initial discharge capacity of 1311 mAh g^{-1} at 0.2C and approximately 95% of the initial discharge capacity was maintained after 100 galvanostatic cycles, resulting in excellent capacity retention with minimal capacity decay of 0.050% per cycle. Furthermore, CC@CeO_2@Li_2S_6 delivered a superior initial discharge capacity of 852.7 mAh g^{-1} at 1C and demonstrated a well-maintained reversible capacity of 852.7 mAh g^{-1} after 220 galvanostatic cycles, leading to surprisingly outstanding capacity retention and cycling stability with zero capacity decay. Moreover, various characterizations and control group experiments were carried out to provide more insights on the underlying mechanisms involved in this work.

2. Experimental section

2.1. Preparation of CC@CeO_2

The preparation of free-standing carbon cloth (CC) with CeO_2 nanorods decoration was achieved by a simple one-step hydrothermal method. Typically, 8 mL of 6 M aqueous NaOH (VWR, 99%) was poured into 88 mL of 0.1 M $Ce(NO_3)_3$•$6H_2O$ (Acros Organics, 99.5%) solution and subsequently the mixture was stirred vigorously before the mixed solution was transferred into a 200 mL Teflon-lined autoclave with CC at the bottom. One-step hydrothermal synthesis was implemented in a programmable box furnace at 90 °C with a dwell time of 48 h to obtain rod-like CeO_2 nanocrystals. After the hydrothermal reaction, the autoclave was cooled down to room temperature, CC decorated with CeO_2 nanorods was collected and rinsed with DI water to completely remove Na^+ and other residual ions. After washing, the CC was placed in vacuum drying oven and CC@CeO_2 was acquired after drying at 60 °C overnight.

2.2. Preparation of Al@S

Conventional Al@S electrode was prepared by mixing 70 wt% of sublimed sulfur powder, 20 wt% of super P carbon black and 10 wt% of PVDF with NMP to form a slurry. The obtained slurry was stirred overnight and subsequently pasted onto aluminum foil. The coated aluminum foil was transferred into a vacuum drying oven and then dried at 60 °C overnight under vacuum.

2.3. Preparation of Li_2S_6-containing catholyte solution and polysulfide adsorption test

Li_2S_6-containing catholyte solution (Li_2S_6) was prepared by directly mixing sublimed elemental sulfur with stoichiometric Li_2S in a liquid organic electrolyte containing 1-M lithium bis(trifluoromethane) sulfonimide (LiTFSI) (Adipogen Corp Ms,

≥ 99%) and 0.5-M $LiNO_3$ (Alfa Aesar, 99.999%) in dioxolane:dimethoxyethane (DOL:DME) (1:1 by volume) (Alfa Aesar, 99%). Sublimed elemental sulfur powder (Alfa Aesar, ≥ 99.5%) and Li_2S (Alfa Aesar, ≥ 99.9%) with a molar ratio of 5:1 were dispersed into the previously obtained organic electrolyte to make 1-M Li_2S_6 catholyte solution (the molar concentrations were precisely calculated based on sulfur). To completely dissolve sulfur and Li_2S, the previously obtained mixed solution was heated on a hot plate at 60 °C for 24 h with vigorously stirring inside of Argon-filled glovebox. The final solution had a reddish color without apparent sediment. To conduct visualized polysulfide adsorption test, the previously obtained 1 M polysulfide solution was diluted to 3 mM Li_2S_6 solution. 25 mg of CeO_2 nanorods powder and bare CC were placed separately into 2 mL of 3 mM Li_2S_6 solution. Photos were taken at the beginning of the test and after 1 h of adsorption.

2.4. Cell assembly

The previously obtained CC@CeO_2, Al@S and bare CC were punched out into circular disks with 15 mm diameter. The sulfur loading of each Al@S disk was controlled to be approximately 1.0–1.2 mg cm^{-2}. The circular disks of CC@CeO_2 and bare CC were coated with slurry containing conductive additive and binder prepared by mechanically mixing super P carbon black (Alfa Aesar, ≥ 99%) and polyvinylidene fluoride (PVDF) in the N-methyl-2-pyrrolidone (NMP) solvent, which was followed by vacuum drying at 60 °C overnight. The CR2032 coin-type cell assembly was completed in an Argon-filled glovebox, and the oxygen and moisture levels were maintained lower than 0.1 ppm. Coated CC@CeO_2 disks, coated CC disks and Al@S disks were used as three investigated cathodes in this work. Lithium metal and Celgard 2400 membrane were used as the anode and the separator, respectively. CC@CeO_2@Li_2S_6 was obtained by implementing the following steps: 9 μL of Li_2S_6-containing catholyte solution was dropped onto one circular CC@CeO_2 disk used as the cathode achieving an areal sulfur loading of 1 mg cm^{-2}. Then, 31 μL of the electrolyte was dropped onto the cathode. Next, the separator was placed on the top of the cathode, which was followed by adding another 31 μL of the electrolyte. Finally, the separator was covered by the lithium metal anode. The same procedure was conducted for circular CC disk to obtain CC@Li_2S_6 and an areal sulfur loading of 1 mg cm^{-2} was also achieved. However, Li_2S_6-containing catholyte was not dropped onto Al@S disk due to the included active material sulfur. The rest of the procedure was remained consistent for Al@S.

2.5. Morphological characterization

The morphological characterization of the samples was implemented by using scanning electron microscopy (SEM, JEOL 7000 FE), transmission electron microscopy (TEM, FEI Tecnai F-20), X-ray diffraction (Philips X'Pert MPD diffractometer) and X-ray photoelectron spectroscopy (XPS, Kratos Axis Ultra DLD).

2.6. Electrochemical measurements

Galvanostatic charge-discharge cycling was carried out on MTI battery tester within a voltage window of 1.7–2.8 V with various current densities (1C = 1675 mAh g^{-1}). Cyclic voltammetry (CV) measurement ranging from 1.7 to 2.8 V at 0.1 mV s^{-1} was implemented on Gamry workstation. Electrochemical impedance spectroscopy (EIS) measurement with the frequency range of 0.01–10^5 Hz was conducted on Gamry Instrument. All the electrochemical measurements were implemented at room temperature (20 °C).

3. Results and discussion

3.1. Morphological characterization prior to galvanostatic cycling

The preparation of free-standing carbon cloth (CC) with decorated CeO_2 nanorods (hereinafter referred to as CC@CeO_2) is schematically illustrated in Fig. 1, and its detailed preparation procedure can be obtained from the experimental section. Scanning electron microscope (SEM) and transmission electron microscope (TEM) were used to characterize the morphologies and sizes of bare carbon cloth, CC@CeO_2 and individual CeO_2 nanorods. In contrast to the smooth surface of individual carbon nanofibers (Fig. 2a) constituting the bare carbon cloth, a series of enlarged SEM images of individual carbon nanofibers decorated with CeO_2 nanorods (Fig. 2b,c) exhibit rough surface of carbon cloth and reasonably well distributed and coated CeO_2 on carbon fibers. As shown in Fig. S1 a, free-standing carbon cloth is recognized as one of the most favorable frameworks to accommodate sulfur. As exhibited in Fig. S1 b,c, carbon cloth can be easily bent and return to its original shape after being deformed without any cracks formed, exhibiting superb mechanical property. Interwoven free-standing carbon cloth consisting of individual carbon fibers framework is also shown in Fig. S1 d,e. The interwoven freestanding carbon cloth (Fig. S1 d,e) with excellent mechanical flexibility and hierarchical porous structure offers sufficient free space to effectively offset the parasitic volume variation of active materials during charge-discharge cycling [22]. Additionally, effectively physical restriction of polysulfide diffusion can be successfully achieved by freestanding interwoven carbon cloth with multi-functional hierarchical porous structure covering the entire framework [23]. However, physical confinement of polysulfide diffusion enabled by non-polar carbon cloth is considered as weak interaction resulting in poor chemical affinity, which cannot guarantee stable adhesion against polysulfides during long cycles and will eventually lead to the capacity decay and cycling instability [7]. As exhibited in Fig. 2b,c, CeO_2 nanorods synthesized via a simple and facile one-step hydrothermal method are uniformly and densely covered onto individual nanofibers of free-standing carbon cloth. Elemental mapping analysis via energy dispersive X-ray spectroscopy (EDS) was conducted to confirm that CeO_2 nanorods was successfully covered onto the individual nanofibers of interwoven carbon cloth and Ce element was homogeneously distributed throughout the entire framework as demonstrated in Fig. 2d–f. Noticeable rod-like features of CeO_2 nanocrystals were clearly seen from the representative TEM images of CeO_2 nanorods (Fig. 2g–i).

3.2. Electrochemical characterization

The electrochemical performance of the cells assembled with areal sulfur loading of 1 mg cm^{-2} was successfully evaluated in order to determine the role of CeO_2 nanorods decoration and synergistic effect of CeO_2 nanorods combined with free-standing carbon cloth in Li-S battery. To make efficient comparison, in this work, innovatively synthesized cathode consisting of free-standing carbon cloth with CeO_2 nanorods decoration combined with Li_2S_6 catholyte (hereinafter referred to as CC@CeO_2@Li_2S_6), cathode comprising carbon cloth incorporated with Li_2S_6 catholyte (hereinafter referred to as CC@Li_2S_6) and basic cathode consisting of pure sublimed sulfur coated onto Al current collector (hereinafter referred to as Al@S) were assessed by various electrochemical characterizations.

Cyclic voltammetry (CV) measurements ranging from 1.7 to 2.8 V at 0.1 mV s^{-1} were firstly implemented to analyze electrochemical redox performance of the investigated cells during charge discharge cycling process. As exhibited in Fig. 3a, for innovatively fabricated CC@CeO_2@Li_2S_6 electrode, in the 1st scan of

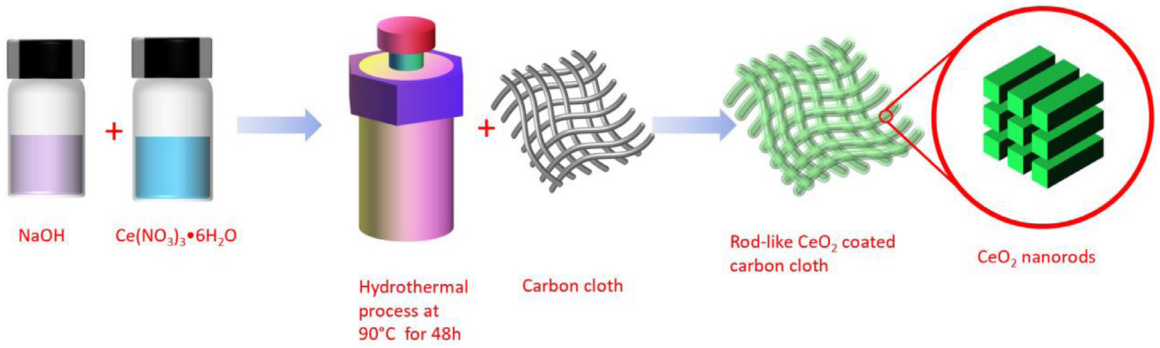

Fig. 1. Schematic diagram of the preparation of carbon cloth coated with CeO_2 nanorods via one-step hydrothermal method.

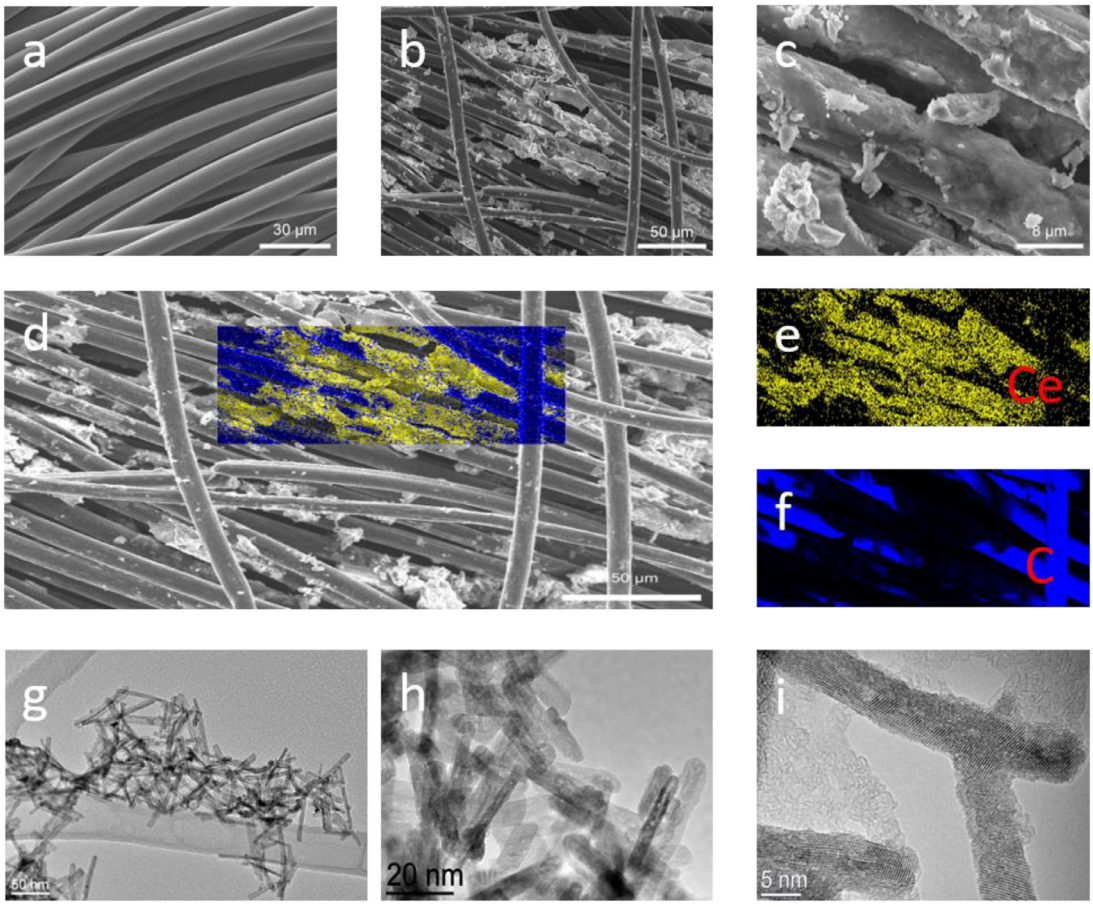

Fig. 2. (a) SEM image of bare carbon cloth consisting of individual nanofibers; (b,c) SEM images of carbon cloth coated with CeO_2 nanorods at different magnifications; (d–f) Elemental mapping of CC@CeO_2; (g–i) TEM images of CeO_2 nanorods at different magnifications.

CV curves, two noticeable cathodic peaks located at 2.30 V and 2.01 V were clearly observed, corresponding to electrochemical conversion from elemental sulfur (S_8) to long-chain soluble polysulfide species (Li_2S_x, $4 \leq x \leq 8$) and electrochemical transformation from long-chain soluble polysulfide species (Li_2S_x, $4 \leq x \leq 8$) to short-chain insoluble Li_2S_2/Li_2S, respectively [24,25]. Two noticeable anodic peaks situated at 2.40 V and 2.44 V were also easily observed in the 1st scan of CV curves, representing the reverse electrochemical conversion from insoluble Li_2S_2/Li_2S to intermediate soluble polysulfide species (Li_2S_x, $4 \leq x \leq 8$) and further to elemental sulfur [26-27]. The CV curves were nearly identical in the following scans, indicating excellent electrochemical reversibility. For CC@Li_2S_6 electrode, as shown in Fig. 3b, two adjacent anodic peaks located at 2.46 V and 2.38 V were observed in the 1st anodic scan and two cathodic peaks situated at 2.27 V and 1.97 V were shown in the 1st cathodic scan. The anodic and cathodic peaks in the following cycles were well overlapped, indicating outstanding cycling reversibility. For conventional Al@S electrode, as shown in Fig. 3c, two cathodic peaks situated at 2.33 V and 2.00 V were shown in the 1st cathodic scan, but only one anodic peak located at 2.47 V was observed in the 1st anodic scan due to severe polarization issue, which slows electronic and ionic transport. These suggest sluggish redox kinetics and weak chemical interaction with polysulfides resulting in parasitic shuttle effect. Fig. 3d exhibits the comparison of the 1st CV curve between CC@CeO_2@Li_2S_6, CC@Li_2S_6 and Al@S electrodes. Two representative cathodic peaks seen from the CV curves of CC@CeO_2@Li_2S_6, CC@Li_2S_6 and Al@S electrodes are denoted as C II (at lower volt-

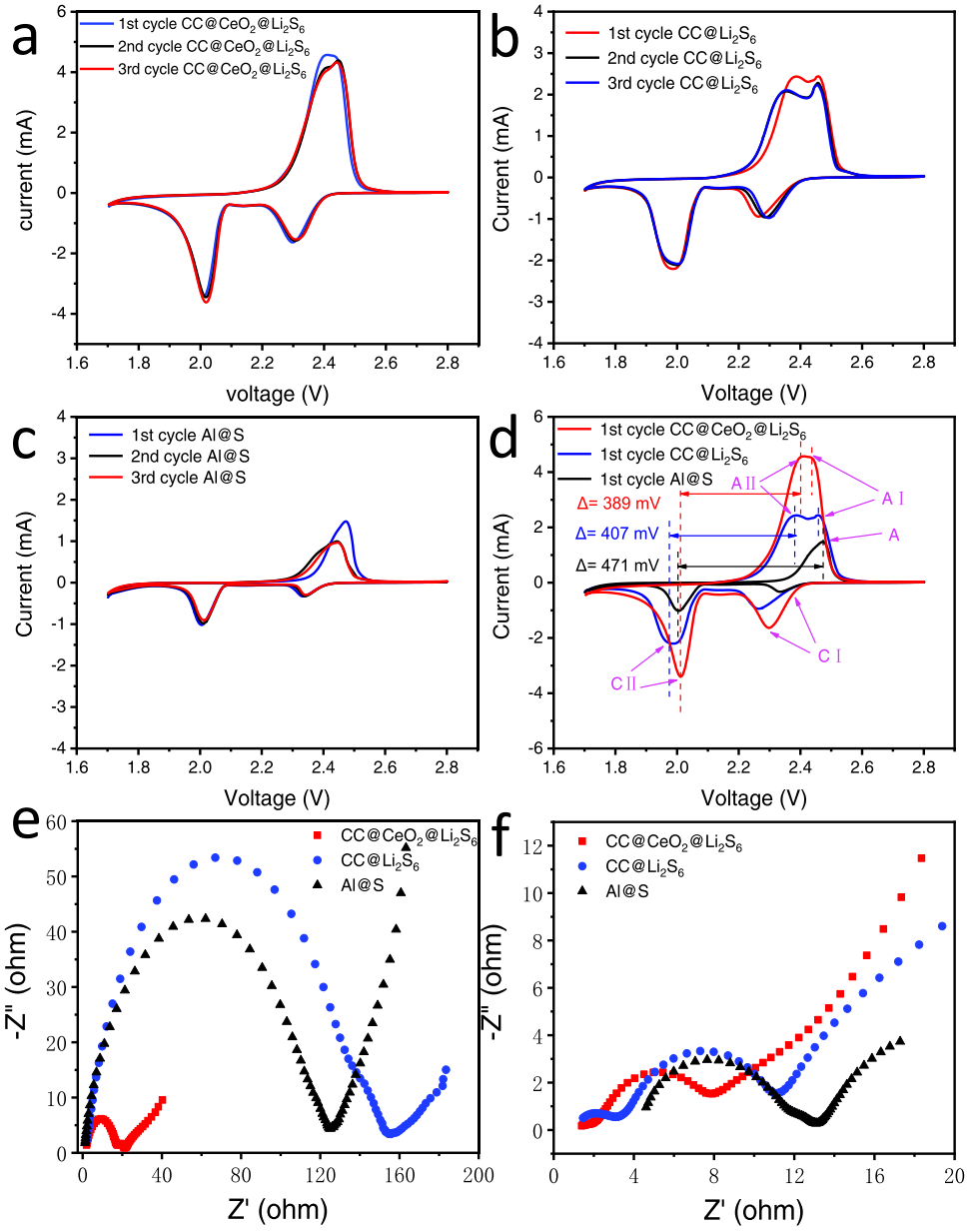

Fig. 3. (a–c) CV curves of $CC@CeO_2@Li_2S_6$, $CC@Li_2S_6$ and Al@S at 0.1 mV s^{-1} ranging from 1.7 to 2.8 V, respectively; (d) The comparison of the 1st cycle CV curves between $CC@CeO_2@Li_2S_6$, $CC@Li_2S_6$ and Al@S; (e) The comparison of EIS for $CC@CeO_2@Li_2S_6$, $CC@Li_2S_6$ and Al@S before cycling; (f) The comparison of EIS for $CC@CeO_2@Li_2S_6$, $CC@Li_2S_6$ and Al@S after 100 galvanostatic cycles at 0.2C.

age potential) and C I (at higher voltage potential). Two typical anodic peaks observed from the CV curves of $CC@CeO_2@Li_2S_6$ and $CC@Li_2S_6$ electrodes are denoted as A II (at lower voltage potential) and A I (at higher voltage potential). Only one anodic peak exhibited from the CV curve of Al@S electrode is referred to as A. It is worth noting that the large portion of discharge capacity of rechargeable LSBs is fulfilled by the electrochemical reduction from soluble long-chain polysulfide species to insoluble short-chain Li_2S_2/Li_2S at lower potential. Therefore, the cathodic peak (C II) located nearby 2.0 V at lower voltage potential plays a more crucial role in electrochemical performance of Li-S battery. The polarization potential of $CC@CeO_2@Li_2S_6$ electrode (389 mV) is smaller than those of $CC@Li_2S_6$ electrode (407 mV) and Al@S electrode (471 mV), indicating strong chemical affinity between CeO_2 nanorods and polysulfides leading to enhanced redox kinetics. The $CC@Li_2S_6$ electrode exhibits 2.42 mA of oxidation current and 2.21 mA of reduction current and Al@S shows 1.50 mA of oxidation current and 1.03 mA of reduction current. For $CC@CeO_2@Li_2S_6$, 4.56 mA of oxidation current peak was obtained, which is significantly sharper and broader, corresponding to approximately 88% higher oxidation current than that of $CC@Li_2S_6$. In addition, for $CC@CeO_2@Li_2S_6$, 3.39 mA of reduction peaks was achieved, which corresponds to approximately 53% higher reduction current than that of $CC@Li_2S_6$ as shown in Fig. 3d, demonstrating exceedingly faster charge transfer and redox kinetics during charge-discharge cycling process [27]. As depicted in **Fig. S2**, in the 2nd scan of CV curves, the polarization potential of $CC@CeO_2@Li_2S_6$ electrode (377 mV) is still much smaller than those of $CC@Li_2S_6$ electrode (381 mV) and Al@S electrode (438 mV). In addition, compared to $CC@Li_2S_6$ with 2.05 mA of oxidation current and 2.01 mA of reduction current and Al@S with 0.99 mA of oxidation current and 0.98 mA of reduction current, for $CC@CeO_2@Li_2S_6$, 4.08 mA of oxidation peak corresponding to approximately 99% higher oxidation current than that of $CC@Li_2S_6$ and 3.47 mA of reduction peaks

corresponding to approximately 73% higher reduction current than that of CC@Li_2S_6 were observed. Electrochemical impedance spectroscopy (EIS) within the frequency range of 0.01 to 10^5 Hz was implemented to further validate the enhanced reaction kinetics and electrochemical performance of three investigated cells. Two depressed semicircles in a high-to-intermediate frequency region were clearly seen for the EIS spectrum of CC@CeO_2@Li_2S_6 (Fig. 3e) before charge-discharge cycling process [28–30], corresponding to the formation of Li_2S_2/Li_2S dense solid film and the charge transfer resistance at the interface between the electrolyte and the electrode, and one nearly straight slope line in the low frequency region associated with the Warburg impedance representing the diffusion process of lithium ions in the organic electrolyte. In contrast, only one depressed semicircle was situated in a high-to-intermediate frequency region for CC@Li_2S_6 and Al@S before cycling, accompanying an oblique line in the low frequency region [29]. Compared with CC@Li_2S_6 and Al@S, significantly reduced internal impedance of CC@CeO_2@Li_2S_6 was resulted from strong affinity of polar CeO_2 nanorods against polysulfide species and effective inhibition of polysulfide diffusion, leading to a fast charge transfer and rapid redox reaction at the interface between the cathode and the liquid electrolyte [29]. It is worth mentioning that considerable reduction in charge transfer resistances of all three investigated cells was observed in Fig. 3f and ascribed to the fact that all three cells were activated after charge discharge cycling [28]. Two depressed semicircles in a high-to-intermediate frequency region and one nearly straight slope line in the low frequency region were clearly seen for the EIS spectrum of cycled CC@Li_2S_6 (Fig. 3f). In contrast, only one depressed semicircle was situated in a high-to-intermediate frequency region and one nearly straight slope line was located in the low frequency region for cycled CC@CeO_2@Li_2S_6 and Al@S electrodes. Elaborately designed CC@CeO_2@Li_2S_6 still exhibited the lowest charge transfer resistance representing a significantly smooth charge transfer compared with CC@Li_2S_6 and Al@S, resulting in faster redox kinetics throughout the entire electrode.

Representative galvanostatic profiles of CC@CeO_2@Li_2S_6, CC@Li_2S_6 and Al@S at low current density of 0.2C are presented in Fig. 4a. Two typical plateaus can be easily seen from the discharge curves of CC@CeO_2@Li_2S_6 and CC@Li_2S_6 electrodes, which is greatly consistent with the CV results. It is well established that the discharge process in Li-S batteries consists of two steps of reduction corresponding to the two distinct voltage plateaus in the representative charge-discharge voltage profile and two distinguishable cathodic peaks in the CV curve. The upper voltage plateau corresponding to the conversion from elemental sulfur (S_8) to long-chain polysulfide (Li_2S_x, $4 \leq x \leq 8$) is located around 2.3 V (vs Li/Li^+), leading to the realization of 25% of a theoretical capacity (0.5 electron transfer per sulfur atom) [31,32]. The lower voltage plateau corresponding to the conversion from long-chain polysulfide (Li_2S_x, $4 \leq x \leq 8$) to insoluble lithium sulfide (Li_2S_2/Li_2S) is situated around 2.1 V (vs Li/Li^+), resulting in the fulfillment of 25% of a theoretical capacity (1.5 electron transfer per sulfur atom) [33]. The only difference between CC@CeO_2@Li_2S_6 and CC@Li_2S_6 is a longer range of the lower voltage plateau provided by CC@CeO_2@Li_2S_6, indicating strong polysulfides adsorption capability of polar CeO_2 nanorods leading to higher active material utilization and excellent capacity retention. CC@CeO_2@Li_2S_6 and CC@Li_2S_6 clearly show two typical voltage plateaus during discharge process, which can be ascribed to the utilization of Li_2S_6-containing catholyte leading to uniform distribution of active material and improved sulfur utilization. In contrast, conventional Al@S is not capable of showing two voltage plateaus of a normal discharge profile due to pulverization of active material. Additionally, another major obstacle that conventionally synthesized elemental sulfur-based cathodes face is that the internal sulfur is not easily accessible to the electrolyte and is difficult to be used immediately, resulting in poor cycling performance in the initial few cycles. This technical issue can be effectively addressed by the introduction of polysulfide-containing catholyte. Long term 100 galvanostatic cycles at 0.2C was carried out to evaluate the cycling stability of CC@CeO_2@Li_2S_6, CC@Li_2S_6 and Al@S and the corresponding results were displayed in Fig. 4b. It can be observed that the initial discharge capacity of CC@CeO_2@Li_2S_6 is up to 1311 mAh g^{-1} at low current density of 0.2C and approximately 95% of the initial discharge capacity is remained after 100 galvanostatic cycles, leading to superior capacity retention with minimal capacity fading of 0.050% per cycle. In contrast, the poor reversible discharge capacities of CC@Li_2S_6 and Al@S are 1044 mAh g^{-1} and 575 mAh g^{-1} respectively resulting from weak non-polar interaction against intermediate polysulfides constructed by bare carbon cloth and conventional Al@S electrode.

To further confirm the effectiveness of CeO_2 nanorods' adsorption capability against intermediate polysulfide species, 1C and 2C measurements of galvanostatic charge-discharge cycling were conducted for CC@CeO_2@Li_2S_6, CC@Li_2S_6 and Al@S. The areal loading of 1 mg cm^{-2} active material sulfur in form of Li_2S_6-containing catholyte solution was applied onto three investigated CC@CeO_2@Li_2S_6, CC@Li_2S_6 and Al@S electrodes. The 1st charge discharge cycling profiles of CC@CeO_2@Li_2S_6, CC@Li_2S_6 and Al@S at 1C were shown in Fig. 4c, exhibiting that innovatively synthesized CC@CeO_2@Li_2S_6 delivers an outstanding discharge capacity of 852 mAh g^{-1}, which is far higher than those of CC@Li_2S_6 and Al@S. The initial discharge capacities of CC@Li_2S_6 and Al@S were only 592 and 134 mAh g^{-1}, respectively. Fig. 4d shows the variation of the discharge capacity and Coulombic efficiency of three investigated cells when being cycled at 1C for 100 cycles. It is worth mentioning that a slight increase in discharge capacity of CC@Li_2S_6 after 60 cycles was observed, which is presumably caused by sluggish activation process of active material polysulfide used in this work [34]. However, CC@CeO_2@Li_2S_6 with strong adsorption capability and better kinetics did not encounter the formidably slow activation process of polysulfide, leading to an outstanding electrochemical reversibility and cycling stability. The Columbic efficiencies of three assembled cells were all close to 100% throughout the 100 cycles of galvanostatic charge-discharge cycling. This promising phenomenon is partly attributed to the addition of 0.5 M $LiNO_3$ into organic electrolyte facilitating the formation of stable solid-electrolyte interface (SEI) layer on the surface of Li metal anode [34]. CC@CeO_2@Li_2S_6 delivered an outstanding initial discharge capacity of 852 mAh g^{-1} and reversible discharge capacity of 866 mAh g^{-1} after 100 cycles. The most stable Columbic efficiency curve was obtained by employing CC@CeO_2@Li_2S_6 presumably due to strong anchoring capability of polar CeO_2 nanorods against polysulfides. A long-term measurement of 220 galvanostatic cycles at 1C rate was carried out on CC@CeO_2@Li_2S_6 with the maintained areal sulfur loading of 1 mg cm^{-2} to obtain deeper insight of capacity retention and cycling stability. Fig. 4e exhibits that innovatively designed CC@CeO_2@Li_2S_6 delivers a high initial discharge capacity of 852.7 mAh g^{-1} and yields an extremely well-maintained reversible capacity of 852.7 mAh g^{-1} even after the long-term 220 galvanostatic cycles, demonstrating the successful restriction of polysulfide enabled by the introduction of CeO_2 nanorods which resulting in surprisingly outstanding capacity retention and cycling stability with near zero capacity fading. As exhibited in Fig. 4f, CC@CeO_2@Li_2S_6 electrode delivered an initial discharge capacity of 776 mAh g^{-1} and a reversible capacity of 677 mAh g^{-1} after 100 cycles with excellent Columbic efficiency of nearly 100%. In contrast, for CC@Li_2S_6 electrode, the phenomenon of electrochemical instability and poor cycling performance occurred after 75 cycles at 2C, which is ascribed to the weak interaction between the non-polar free-standing carbon cloth and polysulfide species,

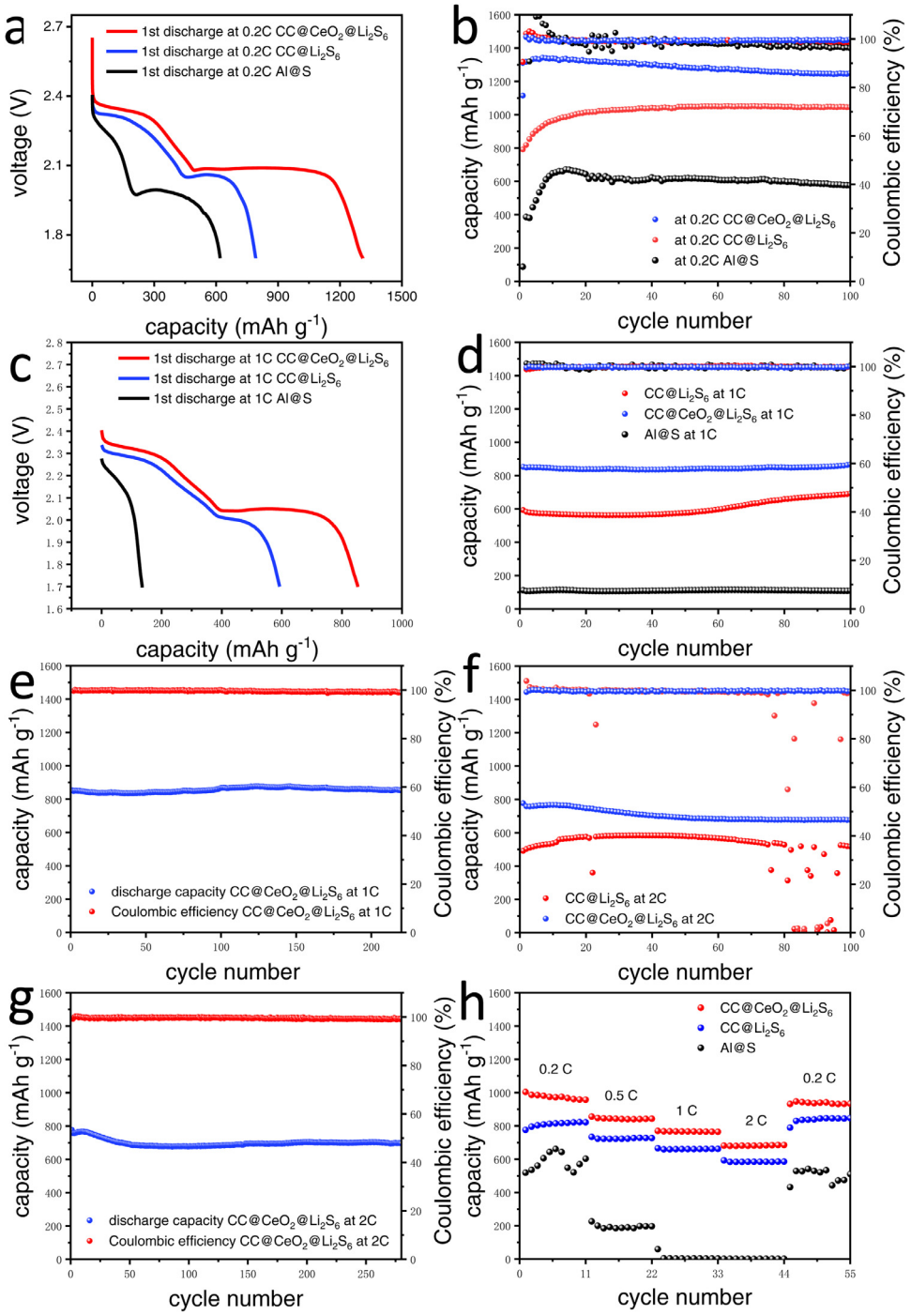

Fig. 4. (a) Initial galvanostatic charge-discharge profiles of $CC@CeO_2@Li_2S_6$, $CC@Li_2S_6$ and Al@S at 0.2C; (b) The comparison of cycling performance and the corresponding Coulombic efficiency between $CC@CeO_2@Li_2S_6$, $CC@Li_2S_6$ and Al@S at 0.2C for 100 cycles; (c) Initial galvanostatic charge-discharge profiles of $CC@CeO_2@Li_2S_6$, $CC@Li_2S_6$ and Al@S at 1C; (d) The comparison of cycling performance and the corresponding Coulombic efficiency between $CC@CeO_2@Li_2S_6$, $CC@Li_2S_6$ and Al@S at 1C for 100 cycles; (e) Superior cycling stability and Columbic efficiency of $CC@CeO_2@Li_2S_6$ at 1C for 220 cycles; (f) The comparison of cycling performance and the corresponding Coulombic efficiency between $CC@CeO_2@Li_2S_6$ and $CC@Li_2S_6$ electrodes at 2C for 100 cycles; (g) Superior cycling stability and Columbic efficiency of $CC@CeO_2@Li_2S_6$ at 2C for 280 cycles; (h) The comparison of rate performance between $CC@CeO_2@Li_2S_6$, $CC@Li_2S_6$ and Al@S.

leading to huge loss of active material. As shown in Fig. 4g, long-term electrochemical test of 280 galvanostatic cycles at high current density of 2C rate was implemented on $CC@CeO_2@Li_2S_6$ electrode to gain more compelling evidence of excellent cycling stability enabled by strong affinity of CeO_2 nanorods against polysulfides. $CC@CeO_2@Li_2S_6$ delivered an initial discharge capacity of 776 mAh g^{-1} and the capacity was eventually maintained at 696 mAh g^{-1} at the end of long-term 280 cycles, providing a superior capacity retention with minimal capacity decay of 0.037% per cycle. The multi-functional architecture also enables $CC@CeO_2@Li_2S_6$ to obtain a superb Coulombic efficiency of nearly 100% throughout the long-term 280 galvanostatic cycles. It is also worth mentioning that $CC@CeO_2@Li_2S_6$ electrode is highly competitive compared to the previously reported Li-S batteries containing CeO_2 (demonstrated in Table S1). Rate performance measurement was also carried out to evaluate the electrochemical stability of assem-

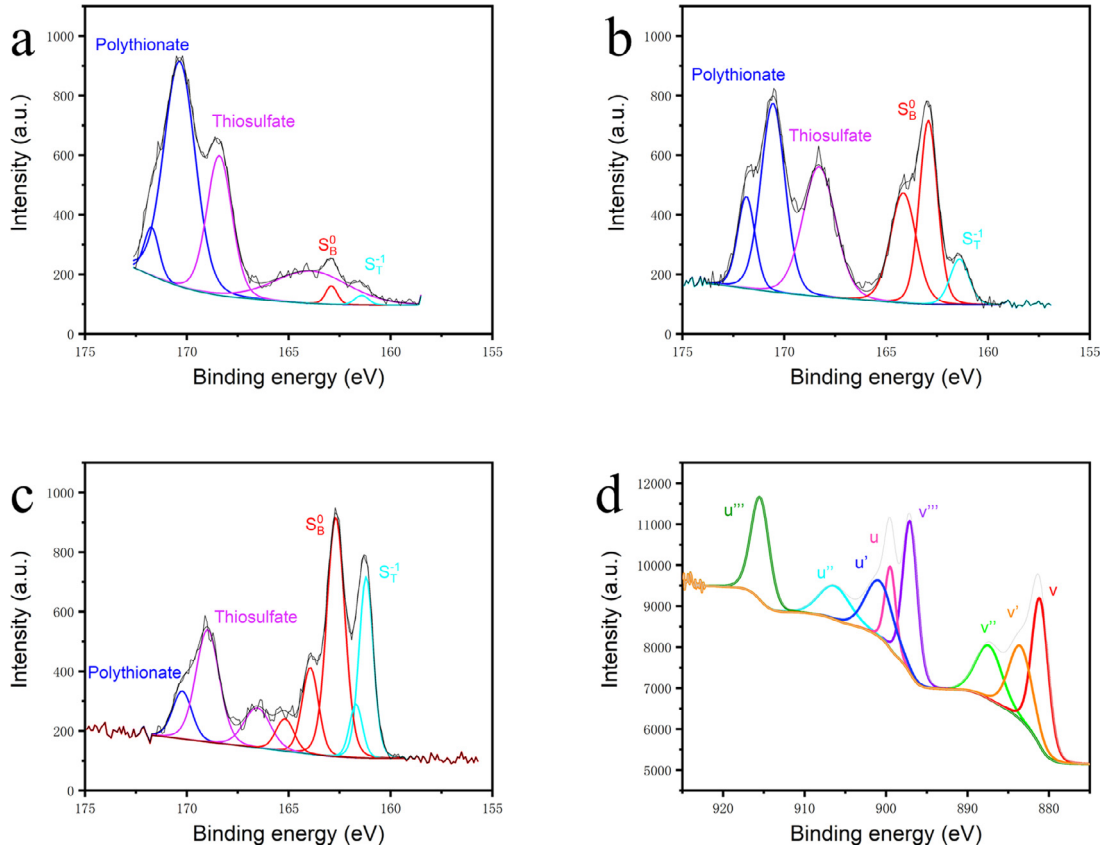

Fig. 5. High-resolution XPS of (a) S 2p spectrum of CC@CeO_2@Li_2S_6 after 100 galvanostatic cycles at 0.2C; (b) S 2p spectrum of CC@Li_2S_6 after 100 galvanostatic cycles at 0.2C; (c) S 2p spectrum of Al@S after 100 galvanostatic cycles at 0.2C; (d) Ce 3d spectrum of CC@CeO_2@Li_2S_6 after 100 galvanostatic cycles at 0.2C.

bled cells tested under different current densities. As demonstrated in Fig. 4h, the obtained CC@CeO_2@Li_2S_6, CC@Li_2S_6 and Al@S electrodes underwent a series of different current densities raised from low current density to high current density (from 0.2C, 0.5C to 1C, 2C) and eventually was reverted back to low current density (0.2C). The assembled cells were tested under each current density for 11 cycles. The highest initial discharge capacity and well-maintained discharge capacity even at a high current density of 2C were obtained by using CC@CeO_2@Li_2S_6. The remarkable rate capability of CC@CeO_2@Li_2S_6 was confirmed by the fact that the discharge capacity did not undergo a significant drop when the current rate increased from 0.2C to 2C and the fact that the discharge capacity was remained pretty close to the initial discharge capacity when the current was reverted back to low current density of 0.2C rate. In stark contrast, replacing CC@CeO_2@Li_2S_6 with Al@S leads to surprisingly poor rate capability, especially under high current density. Initially being cycled at 0.2C and 0.5C and subsequently being cycled at 1C and 2C caused a significant decrease in discharge capacity for Al@S electrode and showed an impressively low capacity under high current density of 1C and 2C. High rate capability was enabled by free standing carbon cloth with 3D interconnected electronic charge transfer pathways and was further enhanced by CeO_2 nanorods with strong affinity against polysulfide species. CC@CeO_2@Li_2S_6 button cell with high areal sulfur loading of 3 mg cm^{-2} and low electrolyte of 40 μL was also assembled. The galvanostatic cycling was performed at 0.2C for 60 cycles as displayed in Fig. S3. The CC@CeO_2@Li_2S_6 electrode with high areal sulfur loading of 3 mg cm^{-2} exhibits an outstanding initial discharge capacity at 0.2C and provides a superior capacity retention with minimal capacity fading.

3.3. XPS and morphological characterization after galvanostatic cycling

X-ray photoelectron spectroscopy (XPS) measurements were carried out to validate the strong chemical interaction between polar CeO_2 nanorods and polysulfides and the obtained results are displayed in Fig. 5a–d. Two distinct peaks with the highest intensity located at 169.7~170.4 eV and 167.7~168.4 eV are attributed to the formation of polythionate and thiosulfate and one single peak with the lowest intensity situated at 161.4~162.8 eV is originated from the terminal sulfur (S_T^{-1}) as exhibited in Fig. 5a [35]. One distinct peak with moderate intensity located at 167.5~168.3 eV is attributed to the formation of thiosulfate, one distinct peak with high intensity situated at 162.9~165.2 eV is originated from the bridging sulfur (S_B^0) of Li_2S_4 and one noticeable peak with moderate intensity located at 160.0~161.4 eV is the contribution from the terminal sulfur (S_T^{-1}) as demonstrated in Fig. 5b [36]. One observable peak with the lowest intensity located at 168.0~168.9 eV is ascribed to the generation of thiosulfate, one noticeable peak with low intensity situated at 164.1~162.7 eV is originated from the bridging sulfur (S_B^0) of Li_2S_4 and one distinct peak with the highest intensity located at 160.8~161.2 eV is the contribution from the terminal sulfur (S_T^{-1}) as demonstrated in Fig. 5c [36].

CeO_2 nanorods with a large amount of electrochemically active oxygen vacancies that can act as efficient polysulfides anchoring sites can achieve facilitated conversion from polysulfide species to thiosulfate [37]. Strong chemical bonding successfully constructed and efficient immobilization of polysulfides accomplished by thiosulfate can further lead to the generation of polythionates that also possess strong chemical adsorption capability, finally resulting in

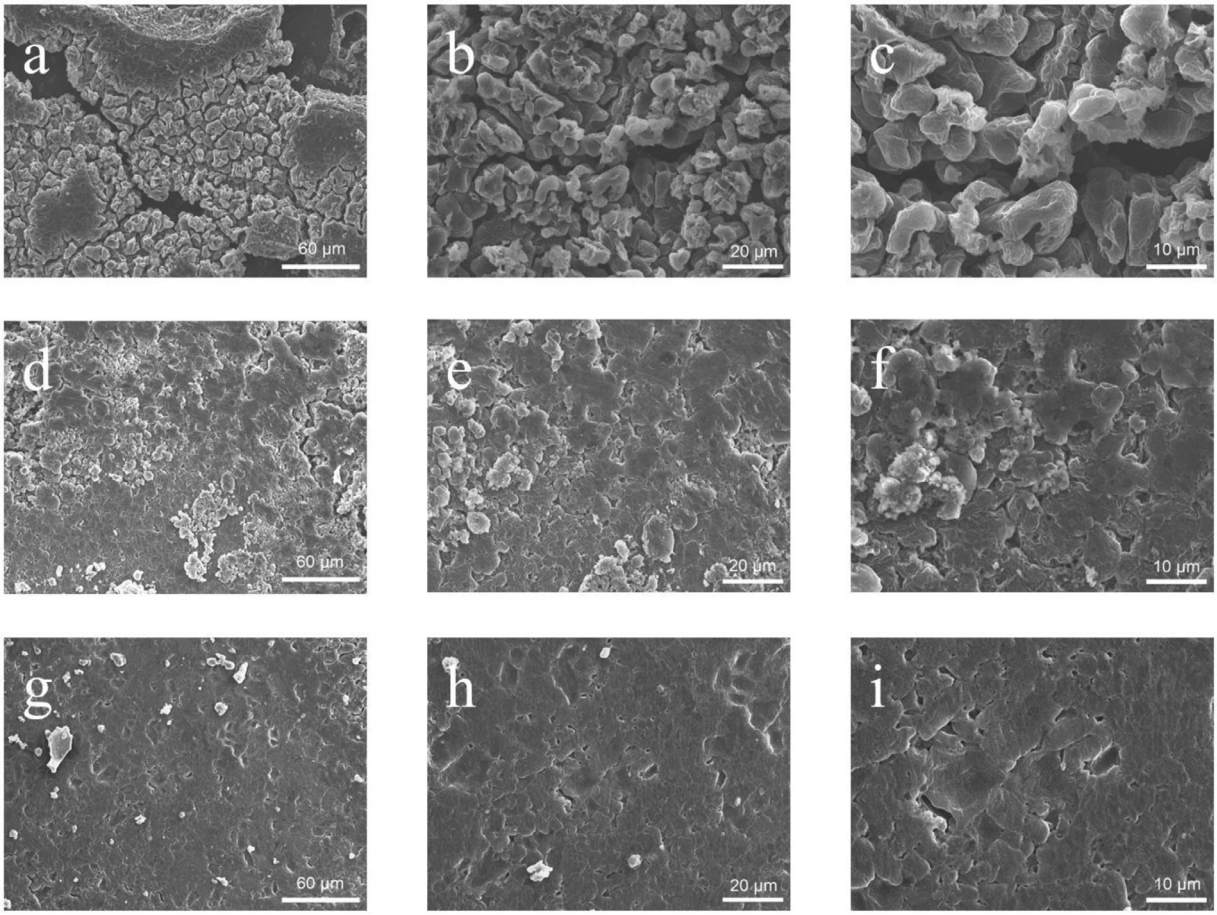

Fig. 6. (a–c) SEM images of Li anode surface from Al@S cell after 100 galvanostatic cycles at low, intermediate, and high magnifications, respectively; (d–f) SEM images of Li anode surface from CC@Li_2S_6 cell after 100 galvanostatic cycles at low, intermediate, and high magnifications, respectively; (g–i) SEM images of Li anode surface from CC@CeO_2@Li_2S_6 cell after 100 galvanostatic cycles at low, intermediate, and high magnifications, respectively.

the formation of insoluble Li_2S_2/Li_2S and the completion of discharge process [37]. Therefore, the largest amount of polythionates and thiosulfates formed during cycling is a clear and convincing evidence that can validate the effectiveness of chemical adsorption ability and facilitated conversion capability towards polysulfides from the addition of CeO_2 nanorods. The spin-orbit splitting of Ce $3d_{5/2}$ and Ce $3d_{3/2}$ denoted as u and v that can be seen from the Ce 3d XPS spectra of CC@CeO_2@Li_2S_6 after cycling was demonstrated in Fig. 5d [38]. Different Ce 4f electron configuration of Ce^{4+}species induces the pairs of peaks u/v, u″/v″ and u‴/v‴, while the couple peaks of u′/v′ represent the two electron configuration of Ce^{3+} species [39]. The reduction from Ce^{4+} to Ce^{3+} during cycling will generate more oxygen vacancies induced by the existence of Ce^{3+}, leading to enhanced chemical adsorption and improved catalytic conversion of polysulfides [39].

A credible confirmation in support of inhibited polysulfide diffusion was achieved by observing the morphological changes of the surface of the Li metal anode from three investigated cells. The three investigated cells were tested under high current density of 1C for repeated 100 galvanostatic cycles and were dissembled inside of Argon-filled glovebox after repeated charge-discharge cycling. The cycled Li metal anodes were rinsed with mixed solution of DME and DOL with volume ratio of 1:1. After drying naturally inside of glovebox, microscopic characterization was implemented by SEM to obtain detailed information about the morphological structure of the surface of three cycled Li metal anodes. From Fig. 6a–c, numerous cracks, serious pulverization and a large amount of Li_2S_2/Li_2S deposition were easily observed on the surface of Li anode from Al@S cell [40], which was related to the side reaction between a large amount of unrestricted polysulfide species and Li metal anode [23]. The parasitic side reaction was mitigated to some extent by using CC@Li_2S_6 electrode, leading to lower amount of cracks and insoluble Li_2S_2/Li_2S formed on the surface of Li metal anode as exhibited in Fig. 6d–f. However, non-polar free standing carbon cloth was not capable of successfully and completely immobilizing polysulfide species that can travel through the electrolyte and reach the Li anode side, which can still cause the formation of cracks and deposited insoluble Li_2S_2/Li_2S on the surface. As demonstrated in Fig. 6g–i, a smooth and nearly intact surface of Li metal anode without obvious pulverization or cracks was observed from CC@CeO_2@Li_2S_6 cell, providing compelling evidence of polysulfides being effectively confined on the cathode side through the strong bonding constructed by CeO_2 nanorods [40].

Cross-sectional SEM images of lithium metal anodes of CC@CeO_2@Li_2S_6, CC@Li_2S_6 and Al@S after cycling and cross-sectional EDS line scans of lithium metal anodes of CC@CeO_2@Li_2S_6, CC@Li_2S_6 and Al@S after cycling are demonstrated in Fig. 7a–i. Al@S demonstrated the maximum thickness of sulfur elemental signals representing occurrence of parasitic shuttle effect as shown in Fig. 7a, d and g. CC@CeO_2@Li_2S_6 exhibited the minimum thickness of sulfur elemental signals indicating minimal polysulfide diffusion and successful immobilization of polysulfides as shown in Fig. 7c, f and i, which is considerably lower than that of CC@Li_2S_6 and Al@S with formidable penetration of sulfur element. These results provide powerful evidence that

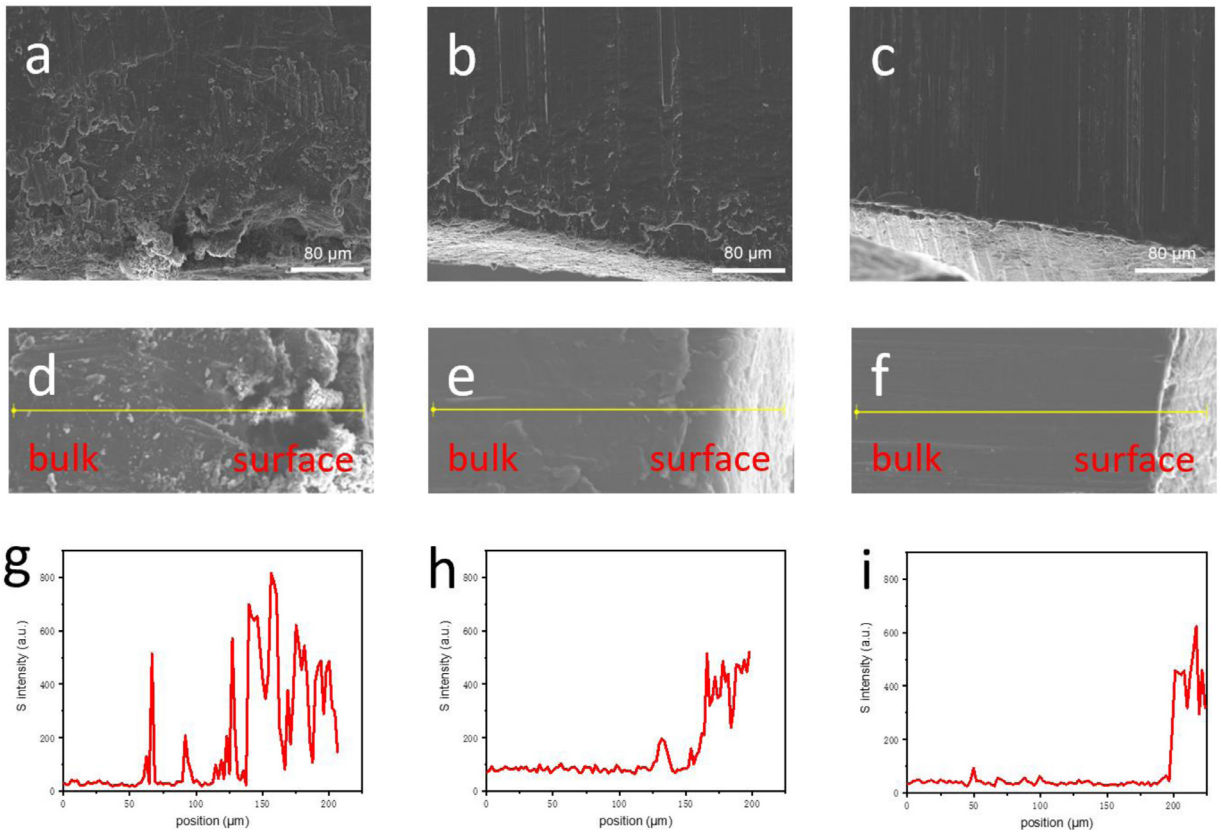

Fig. 7. (a–c) Cross-sectional SEM images of lithium metal anodes of Al@S, CC@Li_2S_6 and CC@CeO_2@Li_2S_6 after 100 galvanostatic cycles at 0.2C; (d–i) Cross-sectional EDS sulfur line scans of lithium metal anodes of Al@S, CC@Li_2S_6 and CC@CeO_2@Li_2S_6.

CC@CeO_2@Li_2S_6 is capable of inhibiting polysulfides diffusion from the cathode side to the lithium metal anode during repeated galvanostatic cycling [41].

3.4. Observation of cycled separators and polysulfides adsorption test

After 100 galvanostatic cycles at high current density of 1C, CC@CeO_2@Li_2S_6, CC@Li_2S_6 and Al@S cells were disassembled inside of Argon-filled glovebox and the separators from three cells were collected. The visual observation of the separators after cycling can be achieved from Fig. 8a–c. The separator obtained from CC@CeO_2@Li_2S_6 cell was clean and fresh indicating minimal polysulfide diffusion and successful immobilization of polysulfides by polar CeO_2 nanorods. The slightly yellow-colored separator collected from CC@Li_2S_6 cell represented that physical restriction of polysulfide diffusion achieved by interwoven carbon cloth can only address the shuttle effect issue to some extent. The heavily yellow-colored separator obtained from Al@S demonstrated serious polysulfide diffusion issue known as shuttle effect, which leading to huge loss of active material, low discharge capacity and formidable cycling instability [42]. Li_2S_6 solution containing CeO_2 nanorods demonstrated an obvious decolorization after 1 h of polysulfide adsorption test compared with Li_2S_6 solution containing non-polar carbon cloth as shown in Fig. 8d,e, indicating superior polysulfide adsorption capability of CeO_2 nanorods which is consistent with the results from other characterization methods [43].

In order to further validate the effectiveness of strong adsorption capability towards polysulfide species achieved by polar CeO_2 nanorods, X-ray diffraction (XRD) was carried out after Li_2S_6 solution adsorption test. As displayed in Fig. 9a, hexagonal carbon was confirmed by three characteristic peaks located at 26.6°, 43.8° and 45.6°, respectively, corresponding to (005), (102) and (103) planes [25]. Carbon is a major component of individual carbon nanofibers. However, no representative peaks of sulfur-related species were shown in the XRD pattern of carbon cloth after Li_2S_6 solution adsorption test, indicating little polysulfides can be effectively adsorbed onto carbon cloth framework and demonstrating poor polysulfides adsorption capability and weak interaction between non-polar carbon cloth and polysulfide species. Cubic CeO_2 was validated by six representative peaks situated at 28.5°, 33.0°, 47.4°, 56.3°, 76.6° and 88.4°, respectively, corresponding to (111), (200), (220), (311), (331) and (422) planes respectively. It is worth mentioning that three characteristic peaks situated at 38.3°, 44.9° and 64.9°, corresponding to (241), (400) and (272) planes respectively of orthorhombic CeS_2 were clearly seen from the XRD pattern of CeO_2 nanorods after Li_2S_6 solution adsorption test as shown in Fig. 9b. The formation of sulfur-containing compound (orthorhombic CeS_2), can provide compelling evidence of strong interaction between polar CeO_2 nanorods and lithium polysulfides. Raman spectroscopy was also conducted to provide additional evidence showing the bonding information between CeO_2 nanorods and lithium polysulfides. As displayed in Fig. 9c, the strongest peak near 454 cm^{-1} can be assigned to triply degenerate F_{2g} mode of fluorite structure of CeO_2 [44]. Moreover, defect-induced peaks near 225 and 600 cm^{-1} correspond to oxygen sublattice disorder and/or oxygen vacancies on the surface of CeO_2 nanorods. After the Li_2S_6 solution adsorption test, the intensity of 200 band decreased significantly, suggesting that the adsorption sites of lithium polysulfides species might be close to the oxygen vacancies or other surface defects on CeO_2 nanorods. The anchoring effect on surface defects of CeO_2 nanorods leads to successful entrapment of intermediate polysulfides species [45]. According to the previously reported work [46], a peak near 1000 cm^{-1} that can be clearly seen from CeO_2 nanorods after Li_2S_6 adsorption test is indicative of

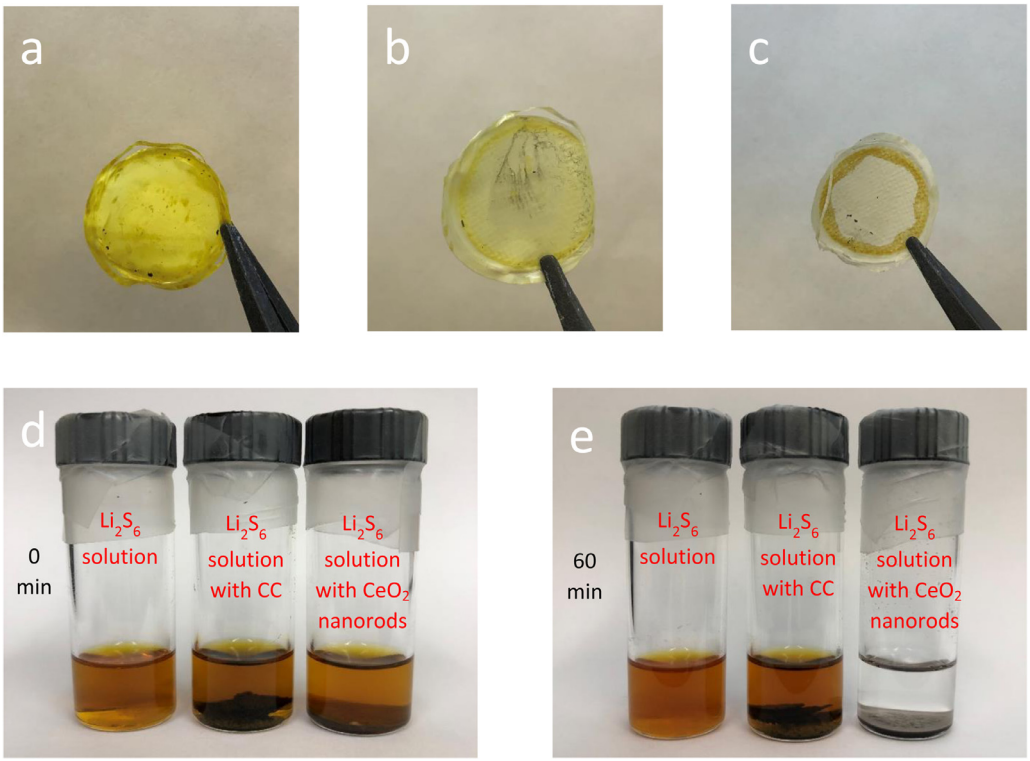

Fig. 8. (a–c) Images of separators collected from Al@S cell, CC@Li_2S_6 cell and CC@CeO_2@Li_2S_6 cell after 100 cycles at 1C; (d,e) Images of Li_2S_6 adsorption test at the beginning and after 1 h.

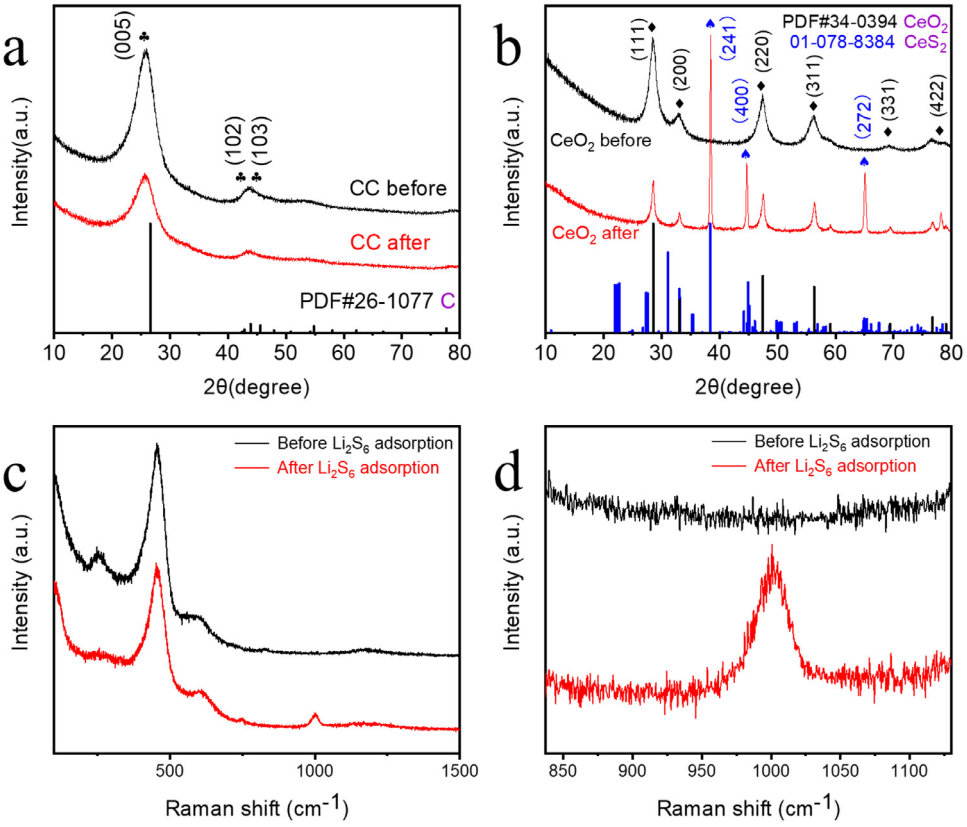

Fig. 9. (a) XRD patterns of non-polar carbon cloth before and after Li_2S_6 solution adsorption test; (b) XRD patterns of polar CeO_2 nanorods before and after Li_2S_6 solution adsorption test; (c) Raman spectra of CeO_2 nanorods before and after Li_2S_6 solution adsorption test and (d) magnified plot of Raman spectra for region of interest.

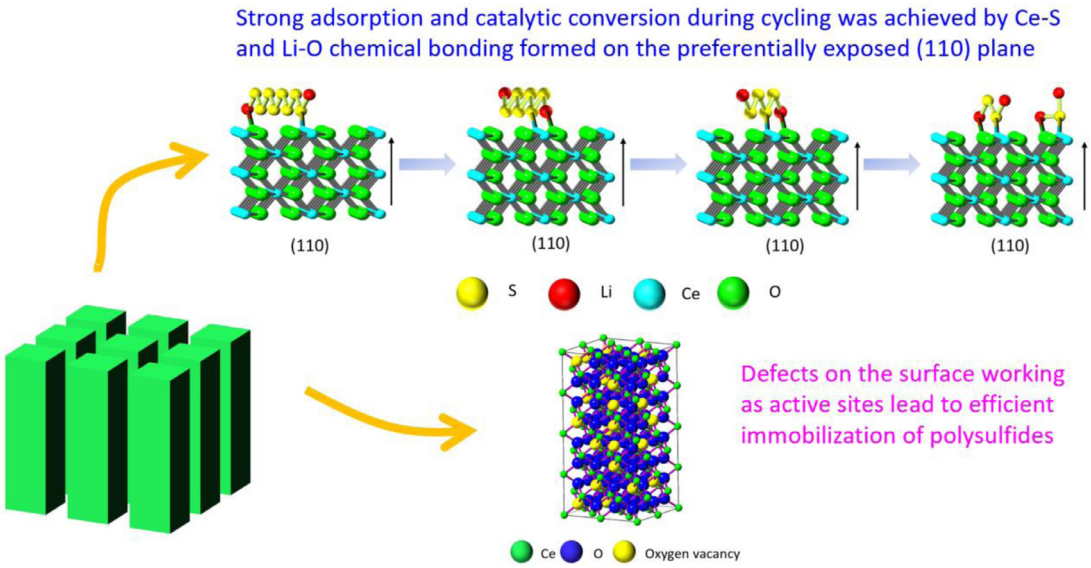

Fig. 10. Schematic illustration of working mechanism of strong adsorption capability of CeO_2 nanorods against polysulfides.

the successful formation of Ce-S chemical bonding as exhibited in Fig. 9d, which is in good agreement with the XRD characterization. Combined with the XRD and Raman spectroscopy results, both entrapment on surface defects and formation of chemical bonding can contribute to the excellent efficiency of CeO_2 nanorods used as host materials of lithium polysulfides in Li-S battery.

The underlying working mechanism involved in this work is schematically illustrated in Fig. 10. Compared to other counterparts of CeO_2 nanorods with various morphologies (nanocubes, nanooctahedra, and nanosphere), CeO_2 nanorods not only possess a variety of surface defects (voids, steps, oxygen vacancy, and Ce^{3+} etc.), but also own more reactive termination surfaces such as {110} and {100}, where mobile oxygen species are accessible on the crystal surface [44,47–49]. According to previously reported DFT simulation of TiO_2 used as host materials [50–54], we propose an underlying working mechanism of Li_2S_6 adsorption where Ce-S and Li-O chemical bonding successfully formed on preferentially exposed (110) crystal plane of CeO_2 nanorods during cycling, leading to efficient inhibition polysulfides diffusion. Compared with CeO_2 octahedra and cubes, more oxygen vacancies formed on the surface of CeO_2 nanorods can be used as efficient polysulfide anchoring sites, ensuring strong polysulfide adsorption capability and realizing successful restriction of polysulfide diffusion, which further leads to superior capacity retention, high Coulombic efficiency and outstanding cycling stability [55–59]. Therefore, CeO_2 nanorods can be a more promising candidate than CeO_2 octahedra and cubes for Li-S battery. Therefore, successful synergy of CeO_2 nanorods covered with abundant oxygen vacancies and Ce^{3+} enabling strong polysulfides adsorption, 3-D interconnected carbon cloth with numerous electron pathways leading to fast reaction kinetics and the utilization of Li_2S_6-containing catholyte resulting in uniform distribution of active material can significantly improve the electrochemical performance of Li-S batteries [60,61].

4. Conclusion

To summarize, CeO_2 nanorods were prepared and successfully anchored onto 3-D interconnected carbon cloth via simple one-step hydrothermal method to serve as a novel host material. Interwoven freestanding carbon cloth can considerably enhance redox kinetics through a 3-D interconnected network with abundant long-range electron transfer channels and can significantly improve redox kinetics by easy accessibility to electrolyte and abundant ion transport pathways. Synergistic effect of free-standing carbon cloth acting as physical confinement against polysulfide and polar CeO_2 nanorods with strong chemisorption capability against polysulfide can provide Li/polysulfide battery with outstanding capacity retention, superb cycling stability and excellent rate capability. Therefore, the 3-D interwoven carbon cloth incorporated with the firmly anchored CeO_2 nanorods and Li_2S_6-containing catholyte ($CC@CeO_2@Li_2S_6$) electrode delivered an initial discharge capacity of 1311 mA h g^{-1} at 0.2C and approximately retained 95% of the initial discharge capacity after 100 galvanostatic cycles, resulting in outstanding capacity retention with capacity fading as low as 0.050% per cycle. Moreover, $CC@CeO_2@Li_2S_6$ delivered an initial discharge capacity of 852.7 mAh g^{-1} at 1C and a high reversible capacity of 852.7 mAh g^{-1} was well maintained after 220 galvanostatic cycles, indicating superior capacity retention and cycling stability with zero capacity decay. This study provides new insights into the morphological tailoring for novel high-efficiency S hosts and effective polysulfide adsorbents to resolve shuttle effect issue and promote the high-performance of Li-S batteries.

Declaration of Competing Interest

The authors declare that they have no known competing financial interests or personal relationships that could have appeared to influence the work reported in this paper.

Credit authorship contribution statement

Zhen Wei: Investigation, Methodology, Formal analysis, Writing – original draft, Writing – review & editing. **Junhao Li:** Formal analysis, Writing – review & editing. **Yifan Wang:** Formal analysis, Writing – review & editing. **Ruigang Wang:** Conceptualization, Investigation, Methodology, Supervision, Formal analysis, Writing – review & editing, Funding acquisition.

Acknowledgment

This work is supported by Alabama Transportation Institute. This project also receives partial financial support from the National Science Foundation (CBET-1856729). The use of TEM and SEM facilities at the Alabama Analytical Research Center (AARC) at The University of Alabama is gratefully acknowledged.

Supplementary materials

Supplementary material associated with this article can be found, in the online version, at doi:10.1016/j.electacta.2021.138645.

Reference

[1] T. Li, X. Bai, U. Gulzar, Y.J. Bai, C. Capiglia, W. Deng, X. Zhou, Z. Liu, Z. Feng, R.P. Zaccaria, A comprehensive understanding of lithium–sulfur battery technology, Adv. Funct. Mater. (2019) 29.

[2] L. Chen, L.L. Shaw, Recent advances in lithium–sulfur batteries, J. Power Sources 267 (2014) 770–783.

[3] A. Rosenman, E. Markevich, G. Salitra, D. Aurbach, A. Garsuch, F.F. Chesneau, Review on Li-sulfur battery systems: an integral perspective, Adv. Energy Mater. 5 (2015).

[4] A. Manthiram, S.H. Chung, C. Zu, Lithium-sulfur batteries: progress and prospects, Adv. Mater. 27 (2015) 1980–2006.

[5] X. Fan, W. Sun, F. Meng, A. Xing, J. Liu, Advanced chemical strategies for lithium–sulfur batteries: a review, Green Energy Environ. 3 (2018) 2–19.

[6] J. Guo, J. Liu, A binder-free electrode architecture design for lithium–sulfur batteries: a review, Nanoscale Adv. 1 (2019) 2104–2122.

[7] F. Li, Q. Liu, J. Hu, Y. Feng, P. He, J. Ma, Recent advances in cathode materials for rechargeable lithium-sulfur batteries, Nanoscale 11 (2019) 15418–15439.

[8] J. Wang, Y. Wu, Z. Shi, C. Wu, Mesoporous carbon with large pore volume and high surface area prepared by a co-assembling route for lithium-sulfur batteries, Electrochim. Acta 144 (2014) 307–314.

[9] J.J. Chen, Q. Zhang, Y.N. Shi, L.L. Qin, Y. Cao, M.S. Zheng, Q.F. Dong, A hierarchical architecture S/MWCNT nanomicrosphere with large pores for lithium sulfur batteries, Phys. Chem. Chem. Phys. 14 (2012) 5376–5382.

[10] J. Zhang, Z. Dong, X. Wang, X. Zhao, J. Tu, Q. Su, G. Du, Sulfur nanocrystals anchored graphene composite with highly improved electrochemical performance for lithium–sulfur batteries, J. Power Sources 270 (2014) 1–8.

[11] Q. Pang, D. Kundu, M. Cuisinier, L.F. Nazar, Surface-enhanced redox chemistry of polysulphides on a metallic and polar host for lithium-sulphur batteries, Nat. Commun. 5 (2014) 4759.

[12] R. Yang, H. Du, Z. Lin, L. Yang, H. Zhu, H. Zhang, Z. Tang, X. Gui, ZnO nanoparticles filled tetrapod-shaped carbon shell for lithium-sulfur batteries, Carbon 141 (2019) 258–265.

[13] L. Fan, H. Wu, X. Wu, M. Wang, J. Cheng, N. Zhang, Y. Feng, K. Sun, Fe-MOF derived jujube pit like Fe_3O_4/C composite as sulfur host for lithium-sulfur battery, Electrochim. Acta 295 (2019) 444–451.

[14] M. Zhu, S. Li, J. Liu, B. Li, Promoting polysulfide conversion by V_2O_3 hollow sphere for enhanced lithium-sulfur battery, Appl. Surf. Sci. 473 (2019) 1002–1008.

[15] S. Yao, H. Tang, M. Liu, L. Chen, M. Jing, X. Shen, T. Li, J. Tan, TiO_2 nanoparticles incorporation in carbon nanofiber as a multi-functional interlayer toward ultralong cycle-life lithium-sulfur batteries, J. Alloy. Compd. 788 (2019) 639–648.

[16] J. Choi, T.-.G. Jeong, D. Lee, S.H. Oh, Y. Jung, Y.-.T. Kim, Enhanced rate capability due to highly active Ta_2O_5 catalysts for lithium sulfur batteries, J. Power Sources 435 (2019).

[17] G. Feng, X. Liu, Z. Wu, Y. Chen, Z. Yang, C. Wu, X. Guo, B. Zhong, W. Xiang, J. Li, Enhancing performance of Li–S batteries by coating separator with MnO @ yeast-derived carbon spheres, J. Alloy. Compd. (2020) 817.

[18] C. Dong, W. Gao, B. Jin, Q. Jiang, Advances in cathode materials for high-performance lithium-sulfur batteries, iScience 6 (2018) 151–198.

[19] G. Yuan, H. Jin, M. Geng, X. Liu, Z. Bakenov, Hybrids of La_2O_3 nanoplates anchored in three-dimensional carbon nanotubes microspheres as efficient sulfur-hosts for highperformance lithium/sulfur batteries, Mater. Lett. 270 (2020).

[20] Y. Zhu, W. Zhao, X. Ye, Supercritical CO_2-assisted fabrication of CeO_2 decorated porous carbon/sulfur composites for high-performance lithium sulfur batteries, SN Appl. Sci. 1 (2019).

[21] H. Wang, B. Zhang, X. Zeng, L. Yan, J. Zheng, M. Ling, Y. Hou, Y. Lu, C. Liang, 3D porous carbon nanofibers with CeO_2-decorated as cathode matrix for high performance lithium-sulfur batteries, J. Power Sources 473 (2020).

[22] X.W. Wu, H. Xie, Q. Deng, H.X. Wang, H. Sheng, Y.X. Yin, W.X. Zhou, R.L. Li, Y.G. Guo, Three-dimensional carbon nanotubes forest/carbon cloth as an efficient electrode for lithium-polysulfide batteries, ACS Appl. Mater. Interfaces 9 (2017) 1553–1561.

[23] J. Yan, X. Liu, H. Qi, W. Li, Y. Zhou, M. Yao, B. Li, High-performance lithium–sulfur batteries with a cost-effective carbon paper electrode and high sulfur-loading, Chem. Mater. 27 (2015) 6394–6401.

[24] F. Zhou, Z. Li, X. Luo, T. Wu, B. Jiang, L.L. Lu, H.B. Yao, M. Antonietti, S.H. Yu, Low cost metal carbide nanocrystals as binding and electrocatalytic sites for high performance Li-S batteries, Nano Lett. 18 (2018) 1035–1043.

[25] Z. Zhang, L.-.L. Kong, S. Liu, G.-.R. Li, X.-.P. Gao, A High-efficiency sulfur/carbon composite based on 3D graphene nanosheet@carbon nanotube matrix as cathode for lithium-sulfur battery, Adv. Energy Mater. 7 (2017).

[26] S. Li, P. Xu, M.K. Aslam, C. Chen, A. Rashid, G. Wang, L. Zhang, B. Mao, Propelling polysulfide conversion for high-loading lithium–sulfur batteries through highly sulfiphilic $NiCo_2S_4$ nanotubes, Energy Storage Mater. 27 (2020) 51–60.

[27] Z.L. Xu, S. Lin, N. Onofrio, L. Zhou, F. Shi, W. Lu, K. Kang, Q. Zhang, S.P. Lau, Exceptional catalytic effects of black phosphorus quantum dots in shuttling-free lithium sulfur batteries, Nat. Commun. 9 (2018) 4164.

[28] Q. Peng, F. Yu, W. Wang, A. Wang, F. Wang, Y. Huang, Ultralight polyethylenimine/porous carbon modified separator as an effective polysulfide-blocking barrier for lithium-sulfur battery, Electrochim. Acta 299 (2019) 749–755.

[29] J. Tu, H. Li, T. Lan, S.-.Z. Zeng, J. Zou, Q. Zhang, X. Zeng, Facile synthesis of TiN nanocrystals/graphene hybrid to chemically suppress the shuttle effect for lithium-sulfur batteries, J. Alloy. Compd. 822 (2020).

[30] X. Gao, Y. Huang, H. Gao, S. Batool, M. Lu, X. Li, Y. Zhang, Sulfur double encapsulated in a porous hollow carbon aerogel with interconnected micropores for advanced lithium-sulfur batteries, J. Alloy. Compd. 834 (2020).

[31] R. Fang, S. Zhao, Z. Sun, D.W. Wang, H.M. Cheng, F. Li, More reliable lithium–sulfur batteries: status, solutions and prospects, Adv. Mater. 29 (2017).

[32] X. Fang, H. Peng, A revolution in electrodes: recent progress in rechargeable lithium-sulfur batteries, Small 11 (2015) 1488–1511.

[33] C.H. Chang, S.H. Chung, A. Manthiram, Effective stabilization of a high-loading sulfur cathode and a lithium-metal anode in Li-S batteries utilizing SWCNT–modulated separators, Small 12 (2016) 174–179.

[34] X. Li, X. Pu, S. Han, M. Liu, C. Du, C. Jiang, X. Huang, T. Liu, W. Hu, Enhanced performances of Li/polysulfide batteries with 3D reduced graphene oxide/carbon nanotube hybrid aerogel as the polysulfide host, Nano Energy 30 (2016) 193–199.

[35] Z. Xiao, Z. Yang, Z. Li, P. Li, R. Wang, Synchronous gains of areal and volumetric capacities in lithium-sulfur batteries promised by flower-like porous Ti_3C_2T x matrix, ACS Nano 13 (2019) 3404–3412.

[36] Y. Luo, N. Luo, W. Kong, H. Wu, K. Wang, S. Fan, W. Duan, J. Wang, Multifunctional interlayer based on molybdenum diphosphide catalyst and carbon nanotube film for lithium-sulfur batteries, Small 14 (2018).

[37] M. Zhang, W. Chen, L. Xue, Y. Jiao, T. Lei, J. Chu, J. Huang, C. Gong, C. Yan, Y. Yan, Y. Hu, X. Wang, J. Xiong, Adsorption-catalysis design in the lithium-sulfur battery, Adv. Energy Mater. 10 (2019).

[38] Y. Peng, C. Wang, J. Li, Structure–activity relationship of VOx/CeO_2 nanorod for NO removal with ammonia, Appl. Catal. B 144 (2014) 538–546.

[39] W. Qi, W. Jiang, F. Xu, J. Jia, C. Yang, B. Cao, Improving confinement and redox kinetics of polysufides through hollow NC@CeO_2 nanospheres for high-performance lithium-sulfur batteries, Chem. Eng. J. 382 (2020).

[40] Z. Zhang, S. Basu, P. Zhu, H. Zhang, A. Shao, N. Koratkar, Z. Yang, Highly sulfiphilic Ni-Fe bimetallic oxide nanoparticles anchored on carbon nanotubes enable effective immobilization and conversion of polysulfides for stable lithium–sulfur batteries, Carbon 142 (2019) 32–39.

[41] G. Zhou, Y. Zhao, C. Zu, A. Manthiram, Free-standing TiO_2 nanowire-embedded graphene hybrid membrane for advanced Li/dissolved polysulfide batteries, Nano Energy 12 (2015) 240–249.

[42] H. Xu, Y. Shi, S. Yang, B. Li, A linear molecule sulfur-rich organic cathode material for high performance lithium–sulfur batteries, J. Power Sources 430 (2019) 210–217.

[43] J. Liu, R. Li, T. Chen, C. Liu, D. Mu, S. Sun, W. Wan, Z. Wang, J. Wei, C. Dai, From bulk to porous: structure transformation of nitrogen and phosphorous co-doped carbon material via sodium chloride assistance and its application in lithium-sulfur batteries, J. Alloy. Compd. 830 (2020).

[44] Z. Liu, J. Li, M. Buettner, R.V. Ranganathan, M. Uddi, R. Wang, Metal-support interactions in CeO_2- and SiO_2-supported cobalt catalysts: effect of support morphology, reducibility, and interfacial configuration, ACS Appl. Mater. Interfaces 11 (2019) 17035–17049.

[45] F. Wang, C. Li, X. Zhang, M. Wei, D.G. Evans, X. Duan, Catalytic behavior of supported Ru nanoparticles on the {1 0 0}, {1 1 0}, and {1 1 1} facet of CeO_2, J. Catal. 329 (2015) 177–186.

[46] B. Mutharani, M. Keerthi, S.M. Chen, P. Ranganathan, T.W. Chen, S.Y. Lee, W.H. Chang, One-pot sustainable synthesis of Ce_2S_3/Gum Arabic carbon flower nanocomposites for the detection of insecticide imidacloprid, ACS Appl. Mater. Interfaces 12 (2020) 4980–4988.

[47] R. Wang, R. Dangerfield, Seed-mediated synthesis of shape-controlled CeO_2nanocrystals, RSC Adv. 4 (2014) 3615–3620.

[48] Z. Liu, J. Li, Q. Ruan, K. Zhang, W. Ma, H. Dong, R. Wang, Probing the optimal thermohydrogen processing conditions of titanium alloy shavings via chemisorption method, Int. J. Hydrog. Energy 43 (2018) 20783–20794.

[49] J. Li, Z. Liu, R. Wang, Support structure and reduction treatment effects on CO oxidation of SiO_2 nanospheres and CeO_2 nanorods supported ruthenium catalysts, J. Colloid Interface Sci. 531 (2018) 204–215.

[50] M. Cheng, T. Han, M. Zhang, H. Zhang, B. Sun, S. Zhu, M. Zhai, Y. Wu, J. Liu, Hydrogel and sulfur co-coating on semispherical TiO_2 as polysulfides-immobilized cathodes for high capacity and stable rate performance lithium-sulfur batteries, Appl. Surf. Sci. 513 (2020).

[51] W. Dong, D. Wang, X. Li, Y. Yao, X. Zhao, Z. Wang, H.-.E. Wang, Y. Li, L. Chen, D. Qian, B.L. Su, Bronze TiO_2 as a cathode host for lithium-sulfur batteries, J. Energy Chem. 48 (2020) 259–266.

[52] C. Zha, D. Wu, T. Zhang, J. Wu, H. Chen, A facile and effective sulfur loading method: direct drop of liquid Li_2S_8 on carbon coated TiO_2 nanowire arrays as cathode towards commercializing lithium-sulfur battery, Energy Storage Mater. 17 (2019) 118–125.

[53] G. Chen, J. Li, N. Liu, Y. Zhao, J. Tao, G. Kalimuldina, Z. Bakenov, Y. Zhang, Synthesis of nitrogen-doped oxygen-deficient TiO_2-x/reduced graphene oxide/sulfur microspheres via spray drying process for lithium-sulfur batteries, Electrochim. Acta 326 (2019).

[54] H.E. Wang, K. Yin, N. Qin, X. Zhao, F.J. Xia, Z.Y. Hu, G. Guo, G. Cao, W. Zhang, Oxygen-deficient titanium dioxide as a functional host for lithium–sulfur batteries, J.Mater. Chem. A 7 (2019) 10346–10353.

[55] L. Ma, R. Chen, G. Zhu, Y. Hu, Y. Wang, T. Chen, J. Liu, Z. Jin, Cerium ox-

ide nanocrystal embedded bimodal micromesoporous nitrogen-rich carbon nanospheres as effective sulfur host for lithium-sulfur batteries, ACS Nano 11 (2017) 7274–7283.
[56] D. Xiao, C. Lu, C. Chen, S. Yuan, CeO_2-webbed carbon nanotubes as a highly efficient sulfur host for lithium-sulfur batteries, Energy Storage Mater. 10 (2018) 216–222.
[57] W. Yan, J. Wei, T. Chen, L. Duan, L. Wang, X. Xue, R. Chen, W. Kong, H. Lin, C. Li, Z. Jin, Superstretchable, thermostable and ultrahigh-loading lithium–sulfur batteries based on nanostructural gel cathodes and gel electrolytes, Nano Energy 80 (2021).
[58] L. Ma, H. Lin, W. Zhang, P. Zhao, G. Zhu, Y. Hu, R. Chen, Z. Tie, J. Liu, Z. Jin, Nitrogen-doped carbon nanotube forests planted on cobalt nanoflowers as polysulfide mediator for ultralow self-discharge and high areal-capacity lithium–sulfur batteries, Nano Lett. 18 (2018) 7949–7954.
[59] L. Ma, W. Zhang, L. Wang, Y. Hu, G. Zhu, Y. Wang, R. Chen, T. Chen, Z. Tie, J. Liu, Z. Jin, Strong capillarity, chemisorption, and electrocatalytic capability of crisscrossed nanostraws enabled flexible, high-rate, and long-cycling lithium-sulfur batteries, ACS Nano 12 (2018) 4868–4876.
[60] R. Carter, L. Oakes, N. Muralidharan, A.P. Cohn, A. Douglas, C.L. Pint, Polysulfide Anchoring Mechanism Revealed by Atomic Layer Deposition of V2O5 and Sulfur-Filled Carbon Nanotubes for Lithium-Sulfur Batteries, ACS Appl. Mater. Interfaces 9 (2017) 7185–7192.
[61] C. Sun, C. Hai, Y. Zhou, Y. Shen, X. Li, Y. Sun, G. Zhang, J. Zeng, S. Dong, X. Ren, J. Zheng, J. Mao, K. Dai, Highly catalytic boron nitride nanofiber in situ grown on pretreated ketjenblack as a cathode for enhanced performance of lithium—sulfur batteries, ACS Appl. Energy Mater. 3 (2020) 10841–10853.